

Showcasing the work on two-dimensional materials by the group of Prof. Bettina V. Lotsch, Max Planck Institute for Solid State Research, Stuttgart, and Chemistry Department, University of Munich (LMU), Germany. Cover by Christoph Hohmann, Nanosystems Initiative Munich (NIM).

Title: A facile wet chemistry approach towards unilamellar tin sulfide nanosheets from $\text{Li}_{4x}\text{Sn}_{1-x}\text{S}_2$ solid solutions

Facile production of single-layered tin sulfide nanosheets was achieved by a direct solid-state reaction, followed by quantitative liquid exfoliation in water. This generic approach may be widely applicable to other layered chalcogenides and can be useful for the fabrication of conformal chalcogenide coatings for battery or thin film absorber applications.

As featured in:



See A. Kuhn et al.,
J. Mater. Chem. A, 2014, 2, 6100.



www.rsc.org/MaterialsA

Registered charity number: 207890

A facile wet chemistry approach towards unilamellar tin sulfide nanosheets from $\text{Li}_{4x}\text{Sn}_{1-x}\text{S}_2$ solid solutions†

Cite this: *J. Mater. Chem. A*, 2014, 2, 6100

Alexander Kuhn,^a Tanja Holzmann,^{abc} Jürgen Nuss^a and Bettina V. Lotsch^{*abc}

We report on the facile production of single-layered tin sulfide nanosheets by a direct solid-state reaction, followed by quantitative liquid exfoliation in water. The new solid solution of SnS_2 and Li_2S with composition $\text{Li}_{4x}\text{Sn}_{1-x}\text{S}_2$ serves as a versatile solid-state precursor with tunable relative lithium and tin content. The end member Li_2SnS_3 , corresponding to the solid solution composition $\text{Li}_{3x}[\text{Li}_x\text{Sn}_{1-x}\text{S}_2]$, crystallizes in the well-known A_2BO_3 structure type with mixed Li/Sn layers alternating with pure Li layers in the cationic substructure, which is interleaved with sulfur layers. The bonding in the Li layers can be regarded as ionic, while the Sn–S bonds have substantial covalent character. The resulting inherent anisotropy allows for the facile production of unilamellar chalcogenide nanosheets with thicknesses below 1 nm and lateral sizes of tens of microns, simply by shaking the crystalline precursor in water. The quantitative exfoliation into single-layered nanosheets was confirmed using optical microscopy, AFM, TEM, as well as X-ray diffraction of freestanding films produced from the colloidal suspension by centrifugation. Upon annealing, the as-obtained nanosheets are converted into SnS_2 without sacrificing their favorable dispersion properties in water. The presented method allows for the cheap and scalable production of unilamellar chalcogenide nanosheets for various potential applications, such as in electronic devices, solar cells, sensors, or battery technology. We expect this method to be generic and transferable to the synthesis of other metal chalcogenides. The use of solid solutions as solid-state precursors, featuring a large compositional range and potential for doping with other metals, may ultimately allow for the controlled introduction of defect levels and rational band-gap engineering in nanosheet materials.

Received 18th October 2013
Accepted 14th November 2013

DOI: 10.1039/c3ta14190j

www.rsc.org/MaterialsA

Introduction

In the past decade, two-dimensional (2D) crystals have seen an upsurge of interest, owing to their miniature dimensions along with unique electronic and optical properties.^{1–5} During the last few years, materials beyond graphene, especially transition metal chalcogenides (TMDs), have increasingly entered the focus of researchers.^{2,6,7} Chalcogenide nanosheets, spanning the entire periodic table and covering a host of electronic properties from semiconductors to superconductors, may play a crucial role not only in the development of inexpensive and earth-abundant next-generation technology for transistors,^{8,9} thin film solar cells,¹⁰ or photocatalysts¹¹ – but also in battery technology as fast-chargeable electrode materials.¹²

Among the tin sulfides, there are three common types: SnS , SnS_2 and Sn_2S_3 .¹³ SnS and SnS_2 nanosheets are usually synthesized by bottom-up synthesis,^{14,15} while SnS_2 may be obtained by mechanical exfoliation.⁸ As SnS_2 has a bandgap of 2.21 eV,¹⁶ it has been explored as a high on/off ratio transistor,⁸ photocatalyst,¹¹ or electrode material.¹²

In general, the synthesis of chalcogenide nanosheets follows the two generic strategies already well established for graphene and related materials: bottom-up^{17–19} or top-down approaches. For top-down synthesis, mechanical exfoliation^{1,7,8} and several wet-chemistry based exfoliation methods have been reported. Liquid exfoliation either occurs by Li intercalation and subsequent exfoliation in water,^{20,21} or by sonication in solvents, with or without the presence of surfactants as stabilizing agents.²² All these methods suffer from incomplete exfoliation, producing not only single layers, but rather an – oftentimes broad – distribution of layer thicknesses.

In this study, we report a “green” and efficient exfoliation strategy quantitatively yielding unilamellar nanosheets of a new ternary tin sulfide, simply by pouring the bulk material into water. The precursor, $\text{Li}_{4x}\text{Sn}_{1-x}\text{S}_2$, is composed of layers of $[\text{Sn}_{1-x}\text{S}_2]^{4x-}$ featuring strong intralayer covalent bonding, while the layers are interleaved by Li^+ ions. In water, facile solvation of

^aMax Planck Institute for Solid State Research, Heisenbergstr. 1, 70569 Stuttgart, Germany. E-mail: b.lotsch@fkf.mpg.de

^bDepartment of Chemistry, Ludwig-Maximilians-Universität München, Butenandtstr. 5-13, 81377 München, Germany. E-mail: bettina.lotsch@cup.uni-muenchen.de

^cNanosystems Initiative Munich (NIM) & Center for Nanoscience, Schellingstr. 4, 80799 München, Germany

† Electronic supplementary information (ESI) available: CSD-426848 and CSD-426849. For ESI and crystallographic data in CIF or other electronic format see DOI: 10.1039/c3ta14190j

Li^+ leads to spontaneous swelling and exfoliation of $\text{Li}_{4x}\text{Sn}_{1-x}\text{S}_2$ into single layers without the need for ultrasonic treatment. The high negative surface potential and the resulting repulsive force between the nanosheets effectively prevent restacking, in sharp contrast to most charge-neutral chalcogenide nanosheets.

Experimental

Solid-state synthesis

$\text{Li}_{4x}\text{Sn}_{1-x}\text{S}_2$ was prepared from Li_2S (Alfa Aesar, 99.9%), Sn (Alfa Aesar, 99.995%), and S (Alfa Aesar, 99.5%) *via* a conventional solid-state synthesis. Pellets were pressed from appropriate mixtures of the starting materials and vacuum-sealed in silica tubes. A slight excess of sulfur (30 mg in a tube of approx. 20 ml and 1 g of the material) was used in order to ensure complete oxidation of Sn. For the reaction, the tubes were placed in furnaces and heated to 750 °C (60 K h^{-1}), held at that temperature for several hours and then quenched to room temperature, whereby excess sulfur was condensed on the walls of the silica tube. All steps were carried out under an inert Ar atmosphere or in vacuum.

Exfoliation and production of free-standing films

For exfoliation, the solid-state precursor $\text{Li}_{4x}\text{Sn}_{1-x}\text{S}_2$ was poured into water (1 g l^{-1}) and placed on an orbital shaker (GFL) for a few days. The exfoliability and the time necessary for exfoliation depend on the stoichiometry of the respective bulk material. The orange colloidal nanosheet suspension was stable for several weeks throughout the time of this study; flocculation was never observed. For the production of solid free-standing films, the nanosheet suspension was centrifuged at 15 000 rpm. The supernatant was removed and residual water was evaporated at 100 °C.

X-ray diffraction

Powder X-ray diffraction (XRD) was performed with a STOE Stadi P diffractometer working in Debye–Scherrer geometry with $\text{Mo-K}_{\alpha 1}$ radiation and a Ge(111) monochromator. For the measurement, the crystalline samples were ground and the powder was filled in a glass capillary with a diameter of 0.3 mm under an Ar atmosphere. X-ray diffraction of the freestanding film in a flat sample holder was carried out with two geometries: (i) in transmission mode using the above-mentioned STOE Stadi P diffractometer or (ii) in reflectance mode using a Bruker D8 Advance diffractometer working with $\text{Cu K}_{\alpha 1}$ radiation. Rietveld refinement was performed with the software DifffracPlus TOPAS v4.2 (Bruker AXS). For single-crystal X-ray diffraction, a SMART-APEX CCD X-ray diffractometer (Bruker AXS) working with graphite-monochromated Mo-K_{α} radiation was used. The integration of the reflections was performed with the SAINT software (Bruker AXS). The structure was solved with direct methods and least squares refinement using the SHELXTL program.

Optical microscopy, AFM

The height and lateral dimensions of the nanosheets were analyzed on a silicon wafer covered with a 300 nm thermally grown SiO_2 layer. To adsorb the nanosheets on the wafer

surface, the wafer was dipped into the colloidal suspension and the liquid was blown off the wafer after some seconds. The wafer was pre-examined using an optical microscope (Olympus BX51). Images were recorded with the Olympus Stream Essentials 1.7 software. AFM was performed with a Veeco CP II system. The AFM images were analyzed with the Gwyddion software.

TEM

For TEM, a drop of the colloidal nanosheet suspension was placed on a lacey carbon film/copper grid (Plano) and dried under irradiation of IR light. TEM was performed with a Phillips CM30 ST (300 kV, LaB_6 cathode). Bright field images and selected area electron diffraction (SAED) patterns were recorded with a Gatan CCD camera.

SEM, UV/VIS, ICP-AES, and zeta potential measurements

Both the crystalline precursors and the freestanding nanosheet film were analyzed by scanning electron microscopy (SEM; Vega TS 5130 MM, Tescan) and SEM-EDX using a Si/Li detector (Oxford). Optical diffuse reflectance spectra of the bulk material and the nanosheet pellet were collected at room temperature with a UV-Vis-NIR diffuse reflectance spectrometer (Agilent Technologies, Cary 5000) at a photometric range of 200–800 nm. Powders were prepared in a sample carrier with a quartz glass window at the edge of the integrating sphere with BaSO_4 as the optical standard. Kubelka–Munk spectra were calculated from the reflectance data. ICP-AES was analyzed with a Vista Pro ICP-AES spectrometer. The characteristic wavelengths were separated with an Echelle-Polychromator (Varian, Darmstadt) and detected with a photomultiplier. The zeta potential of the colloidal suspension was determined by a Malvern Nano ZS Zetasizer (Malvern, Worcestershire) at 20 °C in water using the Smoluchowski method.

Results and discussion

Structural characterization of the crystalline precursors

The crystalline precursor $\text{Li}_{4x}\text{Sn}_{1-x}\text{S}_2$ obtained by conventional solid-state synthesis was structurally characterized by means of X-ray diffraction. Single crystals were obtained for the end member of the solid solution, Li_2SnS_3 . Li_2SnS_3 is isostructural with Li_2SnO_3 and crystallizes in the monoclinic space group $C2/c$ (no. 15) with $a = 6.3961(7)$, $b = 11.0893(13)$, $c = 12.4157(14)$, and $\beta = 99.860(2)^\circ$.²³ The crystallographic details are listed in Table S1,† the atomic coordinates are given in Table S2.† Fig. 1A shows the idealized structure of Li_2SnS_3 , neglecting partial disorder of the Li/Sn sublattice. The layered structure – best described as $\text{Li}[\text{Li}_{1/3}\text{Sn}_{2/3}\text{S}_2]$ – is closely related to the delafossite structure, which is often observed for ternary layered oxides or sulfides based on mono- and trivalent-cations. Depending on the synthesis conditions, we obtained Li_2SnS_3 with different degrees of cation ordering (see ESI†). An individual fully ordered $[\text{Li}_{1/3}\text{Sn}_{2/3}\text{S}_2]^-$ layer is shown in Fig. 1B, with the monoclinic unit cell indicated ($C2/c$). Random distribution of Li and Sn in the $\text{Li}_{1/3}\text{Sn}_{2/3}$ layer leads to an average

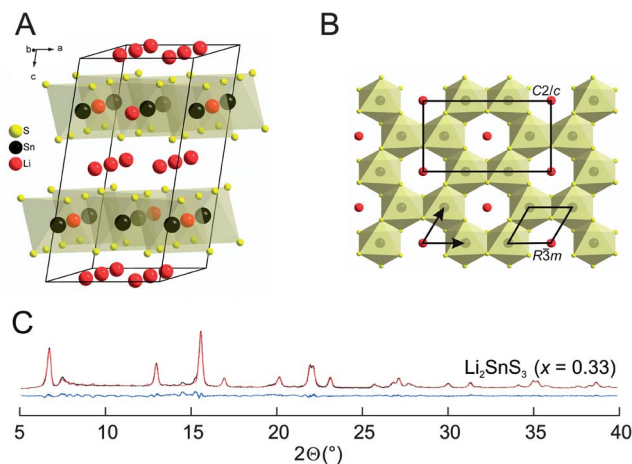


Fig. 1 Crystal structure of Li_2SnS_3 . (A) Idealized fully ordered structure of Li_2SnS_3 crystallizing in the monoclinic space group $C2/c$. (B) Honeycomb structure of an ideal single $[\text{Li}_{1/3}\text{Sn}_{2/3}\text{S}_2]^-$ layer. The arrows mark the translation vectors in the stacking faults leading to the mixed occupancies within these layers in the average rhombohedral structure as discussed in ref. 25. (C): Rietveld refinement of the powder pattern of Li_2SnS_3 (space group $C2/c$).

rhombohedral structure of higher symmetry ($R\bar{3}m$) with a smaller unit cell as indicated in Fig. 1B. This average structure has been observed for many delafossite-type compounds, *e.g.* for the homologous Na_2SnS_3 ,²⁴ and, in our experiments, for melt-quenched Li_2SnS_3 (see ESI†). It was argued in the literature that the apparent disorder results from translational stacking faults of individual layers, according to the two vectors shown in Fig. 1B.²⁵ Note, however, that electron diffraction patterns of individual nanosheets do not show clear superstructure reflections in the $hk0$ plane (see Fig. S7†), as would be expected for an ordered honeycomb-type lattice as implied by Fig. 1B. These results point to the possibility of disorder within individual layers as opposed to disorder due to a superposition structure as a consequence of stacking faults. On the other hand, the Warren-like feature in the XRD pattern of microcrystalline Li_2SnS_3 (Fig. 1C, $7^\circ \leq 2\theta \leq 9^\circ$) suggests stacking faults of at least partially ordered layers along $[001]$ as a reason for the disorder.²⁵ The Rietveld refinement shown in Fig. 1C is based on the monoclinic crystal structure ($C2/c$) obtained from single-crystal X-ray diffraction.

Fig. 2 shows the PXRD patterns of several samples in the $\text{Li}_{4x}\text{Sn}_{1-x}\text{S}_2$ system with $0.11 \leq x \leq 0.33$, whereby $x = 0.33$ corresponds to Li_2SnS_3 and $x = 0$ corresponds to SnS_2 . The formation of a solid solution is hence observed in a wide compositional range and can be understood from Fig. 1 as follows: as one Li atom in the LiSn layer is replaced by a Sn atom, 3 more Li atoms are removed for reasons of charge neutrality, thus decreasing the layer charge density at smaller relative lithium contents. All samples were homogeneous and the crystallites, having a hexagonal morphology, showed the expected Sn : S ratios as measured by SEM-EDX (see Table S3–S6†). A graphical inspection of the XRD patterns of $\text{Li}_{4x}\text{Sn}_{1-x}\text{S}_2$ with $x = 0.25, 0.20$ and 0.11 already reveals that the layered structure is retained for all samples. The monoclinic Li_2SnS_3 ,

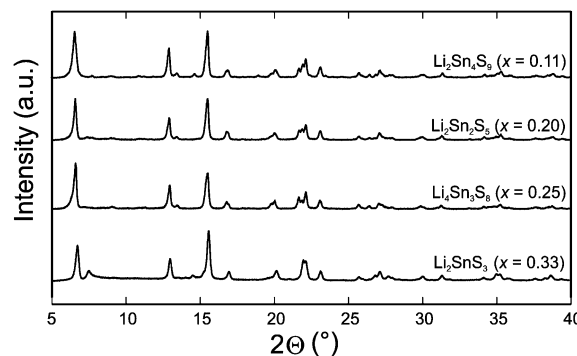


Fig. 2 XRD patterns ($\text{Mo-K}\alpha$) of $\text{Li}_{4x}\text{Sn}_{1-x}\text{S}_2$ with $0.11 \leq x \leq 0.33$. Note the similarity of the upper powder patterns compared to the pattern of Li_2SnS_3 (bottom).

structure model (with slightly different lattice constants) was used as the basis for Rietveld refinements which yielded reasonable structure descriptions for all solid solution members (see ESI Fig. S2†), although some minor reflections point to small amounts of side phases or yet undetermined superstructures, depending on x . Likewise, the Sn : S ratios obtained from the refinements are in good agreement with the expectations. In summary, the solid solution of $\text{Li}_{4x}\text{Sn}_{1-x}\text{S}_2$ exhibits a layered 3R structure best written as $\text{Li}_{3x}[\text{Li}_x\text{Sn}_{1-x}\text{S}_2]$ in a wide compositional range. The structure exhibits alternating layers of (i) $[\text{Sn}_{1-x}\text{S}_2]^{4x-}$ with intralayer covalent bonding resembling the type of bonding in SnS_2 , which is insoluble in water and (ii) Li^+ layers with ionic bonding character, resembling Li_2S , which is soluble in water (see also Fig. 4).

Exfoliation and nanosheet characterization

The crystalline precursor, $\text{Li}_{4x}\text{Sn}_{1-x}\text{S}_2$, can easily be exfoliated in water. A scheme of the proposed exfoliation process is shown in Fig. 4. The success and kinetics of the exfoliation depend on the stoichiometry (see ESI†). While each of the solid solution members can be exfoliated down to the single sheet level, we obtained the best results for $\text{Li}_2\text{Sn}_2\text{S}_5$ ($x = 0.2$), and hence this composition will serve as the basis of our further discussion (see also Fig. 3). Fig. 4 shows the characteristic optical

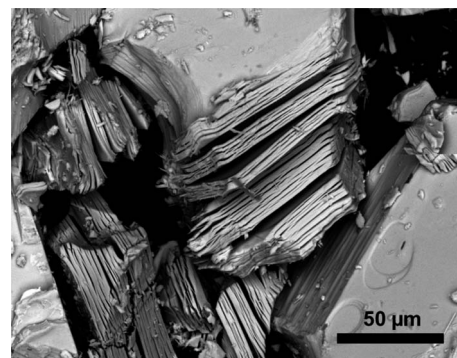


Fig. 3 SEM image of $\text{Li}_2\text{Sn}_2\text{S}_5$ crystals exhibiting a strongly anisotropic, layered crystal morphology with lateral sizes of 20–100 μm .

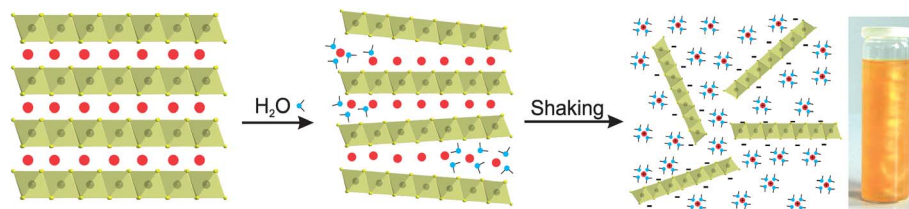


Fig. 4 Scheme outlining the proposed exfoliation mechanism for $\text{Li}_{4x}\text{Sn}_{1-x}\text{S}_2$ and photograph of the obtained colloidal nanosheet suspension ($\text{Li}_2\text{Sn}_2\text{S}_5$, $c = 1 \text{ g l}^{-1}$).

appearance of the obtained colloidal nanosheet suspension with a concentration of 1 g l^{-1} , which is obtained after shaking the crystalline precursor $\text{Li}_2\text{Sn}_2\text{S}_5$ in water for $\approx 6 \text{ h}$. The observed schlieren texture is reminiscent of the formation of orientationally ordered colloidal particles, as seen in liquid crystals. Fig. 5 displays snapshots of the swelling process recorded with an optical microscope (the real-time movie is provided in the ESI, Movie 1†). To observe the exfoliation process, thoroughly ground $\text{Li}_2\text{Sn}_2\text{S}_5$ powder was placed on a microscope slide, followed by a one-drop addition of water. The spontaneous delamination of the crystal corroborates the assumed exfoliation mechanism shown in Fig. 4. Due to the hydration of the lithium cations and the swelling of the crystal the attractive forces between the layers decrease and the crystal eventually delaminates into separate layers.

In order to characterize the morphology and the structure of the dispersed nanosheets, a drop of the colloidal solution of $\text{Li}_2\text{Sn}_2\text{S}_5$ in H_2O was placed on a $\text{Si}/\text{SiO}_2(300 \text{ nm})$ wafer and the deposited nanosheets were analyzed by optical and atomic force microscopy (AFM). Typical images are shown in Fig. 6A and B. The solution consists of well-dispersed single-layer nanosheets with typical lateral sizes of $5\text{--}10 \mu\text{m}$, which is likely determined by the size of the precursor crystallites. The height of the nanosheets as determined from AFM is $8\text{--}10 \text{ \AA}$, which is in good agreement with the expectations for a single-layered nanosheet (theoretical height from the crystal structure of $\text{Li}_2\text{SnS}_3 \approx 7 \text{ \AA}$; Li–Li distance measured along the c -axis). AFM images of

Li_2SnS_3 , $\text{Li}_4\text{Sn}_3\text{S}_8$ and $\text{Li}_2\text{Sn}_4\text{S}_9$ and additional AFM images of $\text{Li}_2\text{Sn}_2\text{S}_5$ after exfoliation in water are shown in Fig. S3–6.† It is worth noting that for $\text{Li}_2\text{Sn}_2\text{S}_5$ we observed only single sheets, whereas for Li_2SnS_3 , $\text{Li}_4\text{Sn}_3\text{S}_8$ and $\text{Li}_2\text{Sn}_4\text{S}_9$ sheets comprising more than one layer were obtained.

TEM was used in order to determine the structure of the nanosheets. Fig. 6C and D show typical images of the $\text{Li}_2\text{Sn}_2\text{S}_5$ nanosheets deposited on a lacey carbon grid of the TEM probe. For higher concentrations, we find several unilamellar nanosheets deposited on top of each another with random orientation (Fig. 6C), while for a lower concentration, the nanosheets tend to crumble and fold during drying (Fig. 6D), presumably due to their large anisotropy. The inset figures show the SAED patterns of the nanosheets. As there are no superstructure reflections observed, the patterns point to a hexagonal plane group for

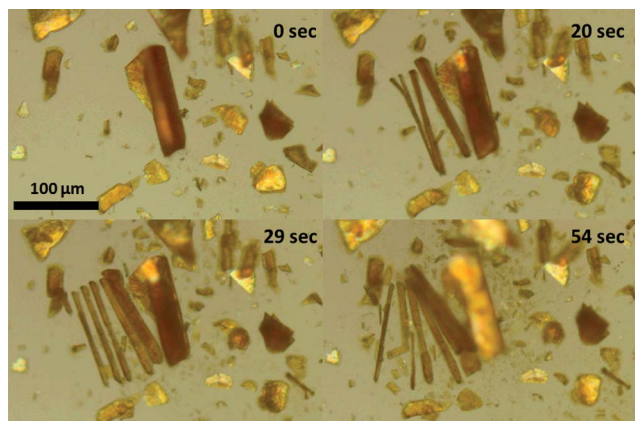


Fig. 5 Exfoliation of $\text{Li}_2\text{Sn}_2\text{S}_5$ in water, recorded with optical microscopy. Time-series images of the spontaneous exfoliation of a $\text{Li}_2\text{Sn}_2\text{S}_5$ crystal after the addition of one drop of water.

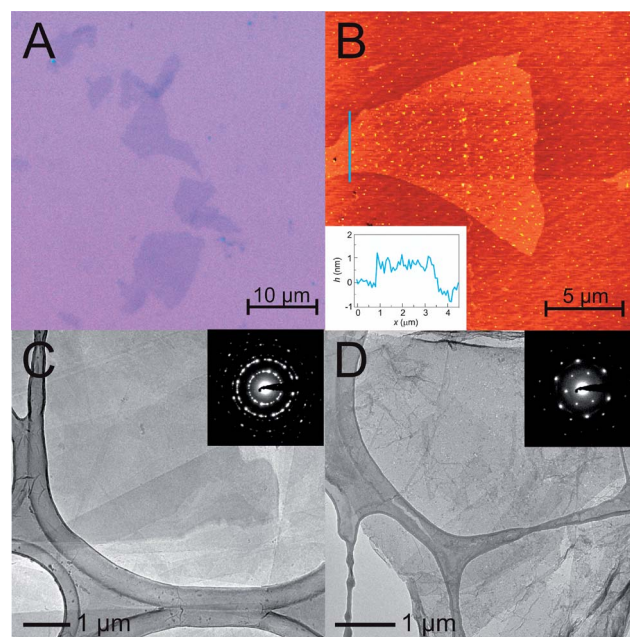


Fig. 6 Characterization of the $[\text{Sn}_2\text{S}_5]^{2-}$ nanosheets. (A) Optical microscope image of the nanosheets deposited on a $\text{Si}/\text{SiO}_2(300 \text{ nm})$ wafer. (B) AFM image of a nanosheet on the same wafer. The inset picture shows the height of the nanosheet of somewhat less than a nanometer, as expected for a single-layer nanosheet. (C and D) TEM images and SAED patterns for stacks of nanosheets (C) and a single (yet crumpled and folded) nanosheet (D). Note the large aspect ratios in all cases.

the structure of the nanosheets – plane group $p3m1$ – which is expected for layers of identical edge-sharing octahedra. This is the case for a random distribution of the Sn vacancies in the $[\text{Sn}_{1-x}\text{S}_2]^{4x-}$ layers. The observed lattice distances are in very good agreement with the expectations from the lattice constants of the crystalline precursors, as discussed in more detail in the next section. In summary, the TEM-SAED results confirm that the $[\text{Sn}_{1-x}\text{S}_2]^{4x-}$ network is retained in the unilamellar nanosheets after exfoliation. Using TEM-EDX, the average Sn : S ratio of the exfoliated single-layer nanosheets was determined to be 29 : 71 – as expected theoretically for $[\text{Sn}_2\text{S}_5]^{2-}$ nanosheets (28.6 : 71.4). The zeta potential of the colloidal suspension of $\text{Li}_2\text{Sn}_2\text{S}_5$ in water was determined at 20 °C after one day, using the Smoluchowski method. A value of -44.7 mV was obtained, which rationalizes the observed excellent long-term stability of the colloidal suspension, as well as the fact that only single sheets seem to be present. This is in sharp contrast to the situation encountered with charge-neutral chalcogenide nanosheets, obtained from either exfoliation by sonication in organic solvents or Li intercalation and subsequent exfoliation in water. For such materials originally bearing no layer charge, a broad thickness distribution of the nanosheets is typically obtained, reflecting the comparably much larger electrostatic stabilization of the nanosheets in the present case.

Formation of freestanding films

We used centrifugation in order to prepare freestanding films from the colloidal nanosheet suspension. Hereby, the supernatant was removed from the slurry on the bottom of the vessel. The XRD pattern of the obtained glue-like nanosheet slurry measured with $\text{Cu-K}_{\alpha 1}$ radiation is shown in Fig. 7A. The pattern features two asymmetric Warren-like reflections which can be assigned to the (01), (10) and the (11) in-plane reflections of the nanosheets in the slurry. The absence of sharp reflections corresponding to the basal spacing in the bulk material clearly supports the picture of complete exfoliation. The slurry was then dried at 100 °C and the freestanding films were produced by centrifugation (see Fig. 7C). In the films, the nanosheets are randomly stacked on top of each other with the sheets being parallel to the top surface of the film, but turbostratically disordered in lateral directions. Fig. 7B shows the X-ray diffraction pattern obtained from the film mounted on a flat sample holder in transmission mode. Hereby, reflections are only measured for planes perpendicular to the sample holder (here: in-plane reflections of the stacked nanosheets). The observed reflections show an asymmetric Warren profile typical of 2D materials – similar to the XRD in Fig. 7A, but with a much better signal-to-noise ratio. As a result of the missing periodicity in the c (*i.e.* stacking) direction, 2D materials are represented by rods along the $[001]$ zone axis in reciprocal

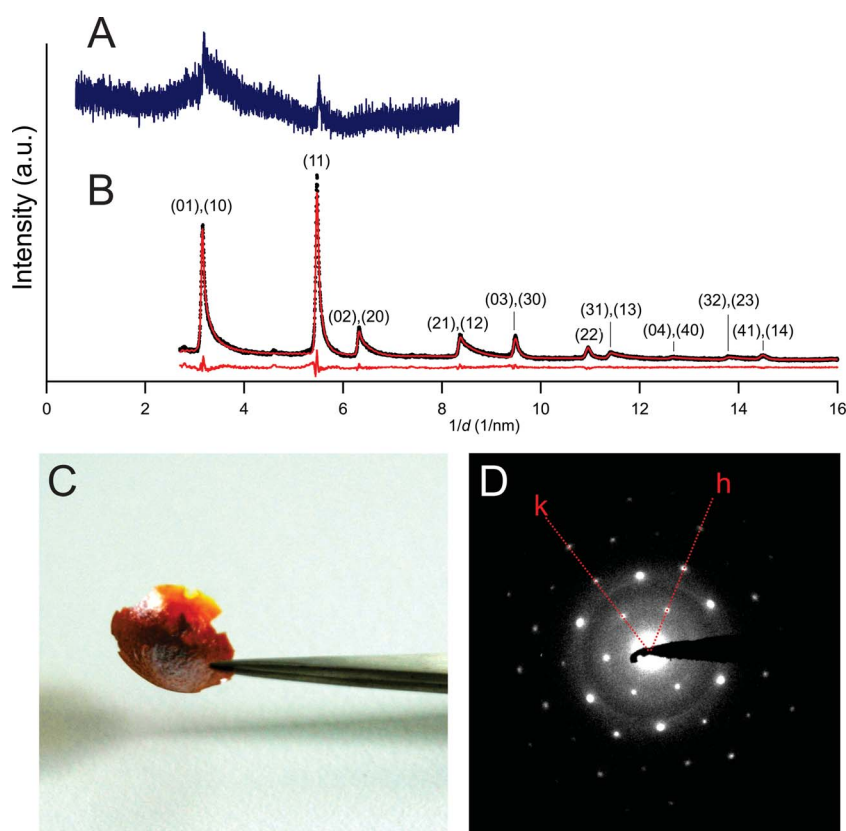


Fig. 7 A) XRD pattern ($\text{Cu-K}_{\alpha 1}$) of the nanosheet slurry obtained after centrifugation at 25 000 rpm (measured in a capillary in Debye–Scherrer mode). B) XRD pattern ($\text{Mo-K}_{\alpha 1}$) of the freestanding nanosheet film shown in (C) with Rietveld refinement (measured in transmission mode). C) Optical appearance of the freestanding film. D) SAED pattern of a single-layered nanosheet (*cf.* Fig. 6), used for indexing.

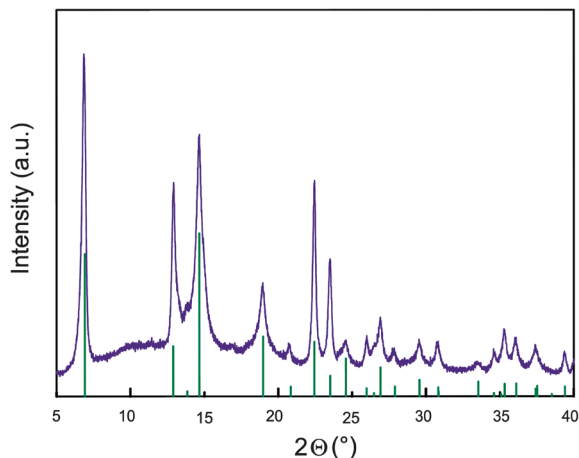
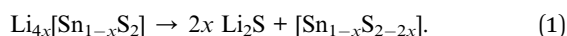


Fig. 8 XRD pattern (Mo- $K_{\alpha 1}$) of the nanosheet pellet after annealing in a vacuum-sealed ampoule at 450 °C (blue line). The green lines are the reference reflections of SnS_2 (space group $P\bar{3}m1$, no. 164).

space, which leads to the asymmetric peaks in the pattern obtained from radial integration of reciprocal space from the origin (*cf.* Fig. S1†).²⁶ For the refinement of the XRD pattern (see Fig. 7B), a single layer of edge-sharing octahedra was assumed with random Li/Sn distribution within the layers. Clearly, the observed and calculated patterns are in very good agreement and the freestanding film consists of randomly stacked 2D layers of edge-sharing octahedra (see ESI† for details of the refinement). The refinement further indicates a Sn : S ratio of 1 : 2 rather than 2 : 5, which is in agreement with the SEM-EDX measurements. Similarly, ICP measurements of the film reveal a depletion in Li down to a Li : Sn ratio of 0.2 : 1 after several washing steps, while the supernatant after centrifugation is enriched in Li (Li : Sn = 4.8 : 1). We therefore propose that Li is formally removed from the sample according to



In line with the concomitant depletion of sulfur we find a lower electron density at the S position in the Rietveld refinement, pointing to a “defective” SnS_2 -type structure. In aqueous solution, the sulfur vacancies may be filled by oxygen giving rise, in essence, to hydrated nanosheets according to



It is worth noting that hydrolysis beyond a Sn : S ratio of 1 : 2 was not observed – in agreement with the fact that SnS_2 is rather stable towards degradation in soft acids.

The above rationale is supported by the observation that after annealing the nanosheet film at 450 °C in a vacuum-sealed ampoule the powder pattern matches with that of SnS_2 (space group $P\bar{3}m1$, no. 164, Fig. 8). Interestingly, in contrast to SnS_2 prepared at high temperatures, our product can readily be redispersed in water, suggesting that the above hydration reaction may operate (eqn (2)).

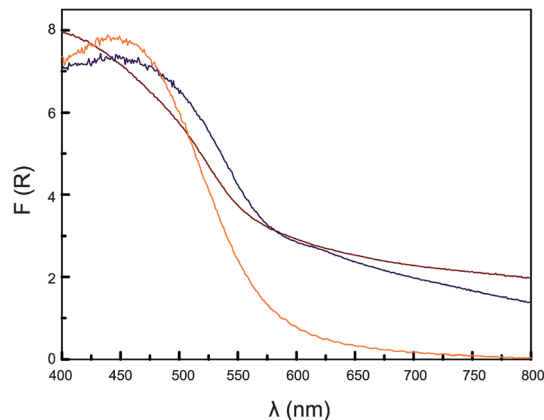


Fig. 9 UV/Vis spectra of bulk $\text{Li}_2\text{Sn}_2\text{S}_5$ (blue line), the nanosheet film after centrifugation and drying (yellow line) and the annealed nanosheet film (brown line). The absorption edges indicate a bandgap of 1.9 eV for the bulk material, 2.1 eV for the nanosheet film and ≈ 1.9 eV for the annealed nanosheet film (see Fig. S10†).

The optical absorption of the crystalline $\text{Li}_2\text{Sn}_2\text{S}_5$, the nanosheet film and the annealed nanosheet film was measured by UV/Vis spectrometry in diffuse reflectance mode (see Fig. 9). In both the crystalline precursor $\text{Li}_2\text{Sn}_2\text{S}_5$ and the annealed nanosheet film the absorption edge points to a bandgap around 1.9 eV. In line with size confinement effects, the nanosheet film displays a slightly larger bandgap of 2.1 eV. All of these values are close to those observed for SnS_2 , which has a bandgap of 2.21 eV,¹⁶ thus again emphasizing the similarity of the above tin sulfide species to the prototype material SnS_2 .

Conclusion

We have demonstrated the efficient production of single-layered tin sulfide nanosheets with large aspect ratios from the crystalline solid solution of $\text{Li}_{4x}\text{Sn}_{1-x}\text{S}_2$. The bonding situation and, hence, the morphology of the layered precursors is inherently anisotropic, giving rise to quantitative exfoliation into unilamellar nanosheets in water without mechanical treatment, organic solvents or additives. Freestanding films have been obtained *via* centrifugation of the nanosheet suspension and transformed into SnS_2 by annealing. We envision that this will enable the fabrication of conformal coatings of tin chalcogenides of desired thickness simply by evaporating the nanosheet suspension. Finally, we expect that the presented exfoliation method, drawing on charge-tunable anionic nanosheets from lithiated solid-solution precursors, will be widely applicable also to other layered chalcogenides.

Acknowledgements

The authors would like to thank V. Duppel for TEM measurements, C. Kamella for SEM-EDX measurements and M.-L. Schreiber for ICP-AES measurements. Financial support by the Max-Planck Society, Nanosystems Initiative Munich (NIM), Center for Nanoscience (CeNS) and Fonds der Chemischen Industrie (FCI) is gratefully acknowledged.

References

- 1 K. S. Novoselov, A. K. Geim, S. V. Morozov, D. Jiang, Y. Zhang, S. V. Dubonos, I. V. Grigorieva and A. A. Firsov, *Science*, 2004, **306**, 666–669.
- 2 M. Chhowalla, H. Suk Shin, G. Eda, L.-J. Li, K. P. Loh and H. Zhang, *Nat. Chem.*, 2013, **5**, 263–275.
- 3 K. S. Novoselov, D. Jiang, F. Schedin, T. J. Booth, V. V. Khotkevich, S. V. Morozov and A. K. Geim, *Proc. Natl. Acad. Sci. U. S. A.*, 2005, **102**, 10451–10453.
- 4 J. A. Roger, M. G. Lagally and R. G. Nuzzo, *Nature*, 2011, **477**, 45–53.
- 5 B. Radisavljevic, A. Radenovic, J. Brivio, V. Giacometti and A. Kis, *Nat. Nanotechnol.*, 2011, **6**, 147–150.
- 6 K. F. Mak, C. Lee, J. Hone, J. Shan and T. F. Heinz, *Phys. Rev. Lett.*, 2010, **105**, 136805.
- 7 A. Splendiani, L. Sun, Y. Zhang, T. Li, J. Kim, C.-Y. Chim, G. Galli and F. Wang, *Nano Lett.*, 2010, **10**, 1271–1275.
- 8 D. De, J. Manongdo, S. See, V. Zhang, A. Guloy and H. Peng, *Nanotechnology*, 2013, **24**, 025202.
- 9 D. B. Mitzi, L. L. Kosbar, C. E. Murray, M. Copel and A. Afzali, *Nature*, 2004, **428**, 299–303.
- 10 J. Britt and C. Ferekides, *Appl. Phys. Lett.*, 1993, **62**, 2851–2852.
- 11 W. Du, D. Deng, Z. Han, W. Xiao, C. Bian and X. Qian, *CrystEngComm*, 2011, **13**, 2071–2076.
- 12 T.-J. Kim, C. Kim, D. Son, M. Choi and B. Park, *J. Power Sources*, 2007, **167**, 529–535.
- 13 R. C. Sharma and Y. A. Chang, *Bull. Alloy Phase Diagrams*, 1986, **7**, 269–273.
- 14 G. Shen, D. Chen, K. Tang, L. Huang, Y. Qian and G. Zhou, *Inorg. Chem. Commun.*, 2003, **6**, 178–180.
- 15 Y. Zhang, J. Lu, S. Shen, H. Xu and Q. Wang, *Chem. Commun.*, 2011, **47**, 5226–5228.
- 16 D. L. Greenaway and R. Nitsche, *J. Phys. Chem. Solids*, 1965, **26**, 1445–1458.
- 17 S. Acharya, B. Das, U. Thupakula, K. Ariga, D. D. Sarma, J. Israelachvili and Y. Golan, *Nano Lett.*, 2013, **13**, 409–415.
- 18 Y. Yu, C. Li, Y. Liu, L. Su, Y. Zhang and L. Cao, *Sci. Rep.*, 2013, **3**, 1866.
- 19 P. Sekar, E. C. Greyson, J. E. Barton and T. W. Odom, *J. Am. Chem. Soc.*, 2005, **127**, 2054–2055.
- 20 P. Joensen, R. F. Frindt and S. R. Morrison, *Mater. Res. Bull.*, 1986, **21**, 457–461.
- 21 Z. Zeng, Z. Yin, X. Huang, H. Li, Q. He, G. Lu, F. Boey and H. Zhang, *Angew. Chem., Int. Ed.*, 2011, **50**, 11093–11097.
- 22 V. Nicolosi, M. Chhowalla, M. G. Kanatzidis, M. S. Srano and J. N. Coleman, *Science*, 2013, **340**, 1226419.
- 23 G. Lang, *Z. Anorg. Allg. Chem.*, 1954, **276**, 77–94.
- 24 W. Mark and O. Lindquist, *Acta Crystallogr., Sect. B: Struct. Sci.*, 1974, **30**, 2620–2628.
- 25 V. Todorova, A. Leineweber, L. Kienle, V. Duppel and M. Jansen, *J. Solid State Chem.*, 2011, **184**, 1112–1119.
- 26 D. Yang and R. F. Frindt, *J. Appl. Phys.*, 1996, **5**, 2376–2385.